VARIATION OF OPTIMAL GAS-SUPPLY CONDITION ALONG WITH DEPOSITION HEIGHT IN DIRECTED ENERGY DEPOSITION

SHIHO TAKEMURA[*], RYO KOIKE[*], YASUHIRO KAKINUMA[*] AND YOHEI ODA[†]

[*] Department of System Design Engineering, Keio University,
3-14-1 Hiyoshi, Kohoku-ku, Yokohama, Kanagawa 223-8522, Japan
e-mail: takemura@ams.sd.keio.ac.jp

[†]DMG MORI CO., LTD,
2-35-16 Meieki, Nakamura-ku, Nagoya, Aichi 450-0002, Japan
e-mail: yo-oda@dmgmori.co.jp

Key words: Directed Energy Deposition, Computational Fluid Dynamics, Inconel 625, Multiphase-flow Simulation

Summary. Directed energy deposition (DED), which is one of additive manufacturing applicable to metals, laminates the material on a baseplate by melting and solidifying with a high-power heat source. In terms of powder-based DED, the material waste tends to be large because powder flow is difficult to converge on the melt pool precisely. This study evaluates the variation in powder distribution when the deposition height is changed in order to obtain the optimal gas-flow rate and powder-nozzle shape. The powder flow is estimated with a computational fluid dynamics simulation based on Euler-Lagrange approach. The simulation results indicate that the proposed nozzles can achieve the high powder convergence stably even if the total amount of gas supply is reduced.

1 INTRODUCTION

Directed energy deposition (DED), which is one of additive manufacturing applicable to metals, attracts various kinds of industries such as aerospace, automotive, and medical products [1]. However, powder-based DED unnecessarily wastes the material because the powder flow is difficult to direct to the melt pool precisely. The powder supply efficiency needs to be stable for the process stability [2] so that the powder flow control is an important issue to enhance the DED's potential for industrial use. In order to improve the powder supply efficiency, it is necessary to analyse the powder distribution under various parameters such as gas-flow rate, powder-nozzle shape and deposit geometry. Therefore, many researchers have been investigating the powder supply process with theoretical and experimental approaches. For example, Pan et al. analysed the gravity-driven metal powder flow in a coaxial nozzle with various gas-flow rates and nozzle geometries [3]. A fluid-dynamics simulation would be helpful

to estimate the powder behavior under the powder nozzle. Although Zhu et al. dealt with the influence of deposition height on the powder distribution with a 2D-axisymmetric model of coaxial nozzle [4], the conventional researches conducted the simulations assuming that the powder flow is free jet, otherwise injected on a flat baseplate [5,6,7]. However, from the practical viewpoint, a detail investigation needs to be conducted considering the variation in the powder flow according to the geometry around the deposition point.

In this study, the powder distribution during the deposition on various heights is numerically evaluated by a computational fluid dynamics (CFD) simulation. To stabilize the powder supply, 3D models including the deposit with various heights are designed, and the influence of carrier gas-flow rate is investigated by analysing the powder-flow around the deposition point. Moreover, the powder-nozzle shape is also discussed along with the CFD simulation results.

2 METHODOLOGY

2.1 Directed energy deposition

In directed energy deposition (DED), the material is laminated on a baseplate by melting and solidifying with a high-power heat source as shown in Fig. 1. In this study, a coaxial powder nozzle initiating a conical powder flow is employed. The powder is supplied to the melt pool by the carrier gas through the outer path of the nozzle. In addition, the shield gas is supplied through the inner path of the nozzle to protect the heat source module. Inert gas like Argon is generally used for carrier and shield gases to prevent the oxidation of deposit. The deposition process can be conducted in all horizontal directions because the coaxial nozzle ensures stable powder supply even when the feed direction is changed [8].

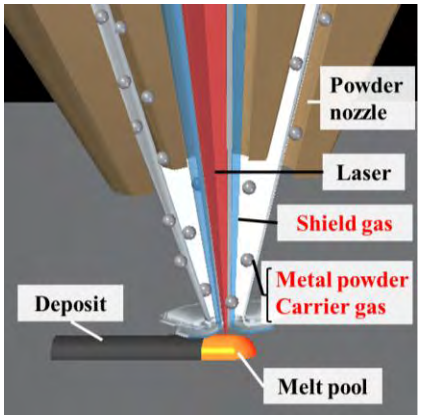

Figure 1: Schematic of DED

2.2 Computational fluid dynamics (CFD) simulation

A gas-solid multiphase-flow simulation is conducted based on the Euler-Lagrange approach.

The gas phase is treated as a turbulent flow and described by a continuity equation and Navier-Stokes equation based on the Reynolds-averaging. The Reynolds-averaged governing equations are given by Eqs. (1) and (2).

$$\frac{\partial \overline{u_i}}{\partial x_i} = 0 \tag{1}$$

$$\frac{\partial \overline{u_i}}{\partial t} + \overline{u_j}\frac{\partial \overline{u_i}}{\partial x_j} = -\frac{1}{\rho}\frac{\partial \bar{p}}{\partial x_i} + \nu\frac{\partial^2 \overline{u_i}}{\partial {x_j}^2} - \frac{\partial \overline{u_i' u_j'}}{\partial x_j} \tag{2}$$

where u_i [m/s] is the flow velocity, x_i [m] is the Cartesian coordinate, t [s] is the time, ρ [kg/m^3] is the density, p [kg/m·s^2] is the pressure, ν [m^2/s] is the kinematic viscosity, and bar denotes the time-averaged value. In Eq. (2), the first and second terms on the left side represent the time term and the convection term, respectively, and the terms on the right side represent

the pressure term, viscosity term, and turbulent diffusion term in order. To complete the equation, modeling of the Reynolds stress $-\rho\overline{u_i{}'u_j{}'}$ is necessary. The Reynolds stress is expressed by using the turbulent viscosity and given as

$$-\rho\overline{u_i{}'u_j{}'} = \mu_t\left(\frac{\partial\overline{u_i}}{\partial x_j}+\frac{\partial\overline{u_j}}{\partial x_i}\right)-\frac{2}{3}\rho k\delta_{ij} \tag{3}$$

where μ_t [kg/(m·s)] is the turbulent viscosity, k [m^2/s^2] is the turbulent kinetic energy and $\delta_{ij} = 1$ for $i = j$, otherwise $\delta_{ij} = 0$. In this study, a k-ε turbulent model, developed by Launder and Spalding [9], is applied to solve the equations. In this model, the turbulent viscosity μ_t is given as Eq. (4).

$$\mu_t = C_\mu\rho\frac{k^2}{\varepsilon} \tag{4}$$

where C_μ is the model constant, ε [m^2/s^3] is the dissipation of kinetic energy of the turbulence. The conservation of the turbulent kinetic energy is expressed as

$$\frac{\partial(\rho k)}{\partial t}+\frac{\partial(\rho k u_i)}{\partial x_i} = \frac{\partial}{\partial x_j}\left\{\left(\mu+\frac{\mu_t}{\sigma_k}\right)\frac{\partial k}{\partial x_j}\right\}+\rho\overline{u_i{}'u_j{}'}\frac{\partial\overline{u_i}}{\partial x_j}-\rho\varepsilon \tag{5}$$

The conservation of the dissipation of kinetic energy of the turbulence is expressed as

$$\frac{\partial(\rho\varepsilon)}{\partial t}+\frac{\partial(\rho\varepsilon u_i)}{\partial x_i} = \frac{\partial}{\partial x_j}\left\{\left(\mu+\frac{\mu_t}{\sigma_\varepsilon}\right)\frac{\partial\varepsilon}{\partial x_j}\right\}+\left(C_{\varepsilon1}\rho\overline{u_i{}'u_j{}'}\frac{\partial\overline{u_i}}{\partial x_j}-C_{\varepsilon2}\rho\varepsilon\right)\frac{\varepsilon}{k} \tag{6}$$

where, $C_\mu = 0.09$, $\sigma_k = 1.0$, $\sigma_\varepsilon = 1.3$, $C_{\varepsilon1} = 1.44$, and $C_{\varepsilon2} = 1.92$ are the empirical constants.

In the Euler-Lagrange approach, the discrete phase is computed by solving a motion equation for each particle. The motion equation is given by Eq. (7).

$$\frac{du_p}{dt} = \frac{u-u_p}{\tau_r}+g\frac{\rho_p-\rho}{\rho_p} \tag{7}$$

where u_p [m/s] is the particle velocity, u [m/s] is the fluid velocity, ρ_p [kg/m^3] is the particle density, ρ [kg/m^3] is the fluid density, τ_r [s] is the particle relaxation time, and g [m/s^2] is the gravitational acceleration. The first and second terms on the left side represent the drag force and the gravitational force respectively. Since the fluid density is much smaller than the particle density ($\rho/\rho_p \ll 1$), the drag force and the gravitational force dominantly work on the particles. Then, the particle relaxation time τ_r is given by

$$\tau_r = \frac{\rho_p d_p^2}{18\mu}\frac{24}{C_d Re_p} \tag{8}$$

where d_p [m] is the particle diameter, μ [kg/(m·s)] is the fluid viscosity. Re_p is the particle Reynolds number and defined as

$$Re_p = \frac{\rho d_p |u_p - u|}{\mu} \tag{9}$$

By solving the Eq. (7), the particle velocity can be obtained. In addition, the particle trajectory can be represented by following Eq. (10).

$$\frac{dx_p}{dt} = u_p \tag{10}$$

where x_p is the position of particle.

3 SIMULATION ASSUMPTIONS AND SETUP

3.1 Simulation assumptions

The CFD simulation in this study is conducted by using ANSYS Fluent (ANSYS, Inc.), and following assumptions are taken into the simulation;

(1) A steady-state gas flow is considered.
(2) Collisions among particles are not considered.
(3) Particle is assumed to be spherical.
(4) Particle size is assumed to follow a Rosin-Rammler distribution.
(5) Any thermal effect like an interaction between particles and the laser is not considered.
(6) At the outlet, the gauge pressure is set to be zero.
(7) At the wall, a no-slip condition is applied.

3.2 Simulation model and setup

The 3D CAD models are created for the CFD simulation as shown in Fig. 2. In order to evaluate the variation in powder distribution along with the deposition height, the CAD models including the deposit are created as shown in (a). In addition, the CAD model only with a baseplate, assuming the first-layer deposition, is also created for comparison as presented in (b). The powder-nozzle shape is based on a five-axial combined machining center (LASERTEC 65 3D, DMG MORI CO., LTD.). As for (a), the geometry of deposit is decided according to the results in preliminary experiments; therefore, the top of deposit is rounded. Figure 3 shows the cross-section of CAD model. In this study, the powder convergence distance L, defined as the height between the nozzle exit and the convergence point of conical powder stream, is 13 mm. The standoff distance S, which is the distance from the nozzle exit to the baseplate, is also set to be 13 mm. Figure 4 shows the boundary conditions for the discrete phase. Particles are escaped from the outlet and trapped at the bottom of the processing area or the top surface of deposit.

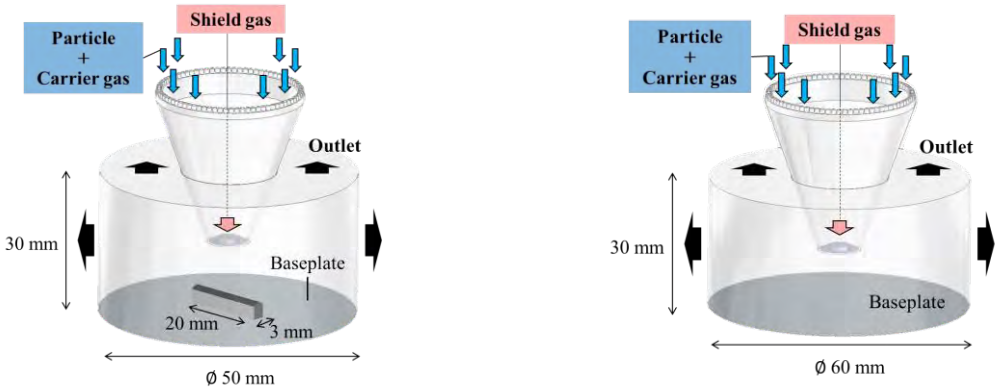

(a) With deposit and baseplate (b) With baseplate (1st-layer of deposition)

Figure 2: CAD model

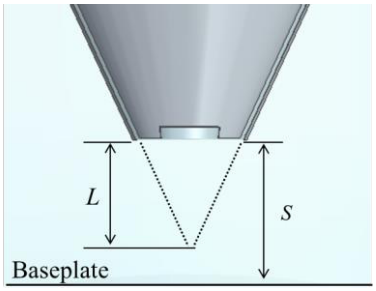

Figure 3: Definition of powder convergence distance (L) and standoff distance (S)

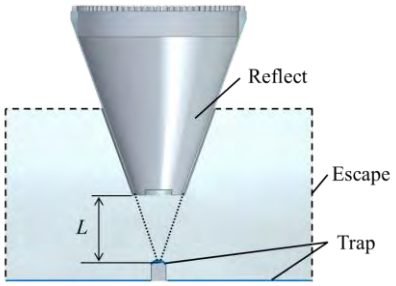

Figure 4: Boundary conditions

In this study, the simulations are conducted with 4 types of carrier gas-flow rate. The CAD models are created with 3 types of deposition height, on a baseplate, 9-layer and 49-layer deposits, i.e., models are assuming the 1st-layer, 10th-layer and 50th-layer depositions, respectively. Other simulation conditions are summarized in Table 1. Physical properties of argon are applied to decide the fluid density and viscosity, and the particle density refers to the density of Inconel 625 alloy.

Table 1: Simulation conditions

Carrier gas-flow rate	L/min	3, 4, 6, 8
Shield gas-flow rate	L/min	4
Powder feed rate	kg/min	18×10^{-3}
Fluid density	kg/m^3	1.784
Fluid viscosity	kg/(m·s)	2.22×10^{-5}
Particle density	kg/m^3	8440
Particle size	μm	53 – 105

4 PARTICLE DISTRIBUTION ON TOP SURFACE OF DEPOSIT AND BASEPLATE

As a result of the simulation, the particle trajectory is obtained as shown in Fig. 5. To clarify the powder convergence, the distribution of trapped particles is mapped corresponding to the XY coordinate. Figure 6 shows the particle distribution viewed from the powder nozzle, when the carrier gas-flow rate is 4 L/min. This result indicates that the particle distribution slightly spreads at the higher layer. Furthermore, the particles are not supplied at the center of the processing point. In order to compare the particle distribution quantitatively, Fig. 7 shows the probability distribution of particles for every 0.1 mm radius from the center of melt pool.

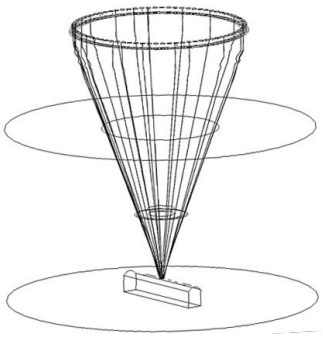

Figure 5: Particle trajectory

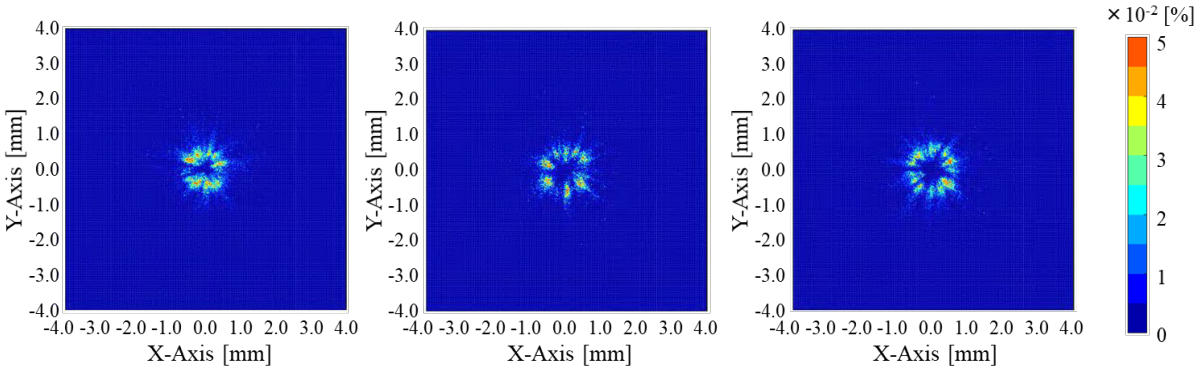

(a) Baseplate (b) 9-layer (c) 49-layer

Figure 6 Particle distribution on top surface of deposit and baseplate (Carrier gas-flow rate : 4 L/min)

Comparing the distributions in Fig. 7 regarding deposition height, more particles distribute at the distant position from the center of melt pool when the deposit is higher, excepting the carrier gas-flow rate of 3 L/min. The variation in gas flow between the nozzle exit and baseplate would influence on the spread of particle distribution. Figure 8 shows the velocity distribution of gas flow at the cross-section of processing area. In (b), the flow spreads on the baseplate below the deposition point. On the other hand, the flow goes to downward along the side surface of deposit in (c). Figures 9 are the enlarged pictures of the nozzle exit in Figs. 8(b), (c). In case of 49-layer shown in Fig. 9(b), the flow near the nozzle exit is slightly goes to downward by comparison with the flow of 9-layer deposition as (a). Figure 10 shows the pressure distribution at the cross-section of processing area, and indicates that the stagnation area gets small when the deposit becomes high. In other words, the flow direction hardly changes around the processing point in 49-layer deposition.

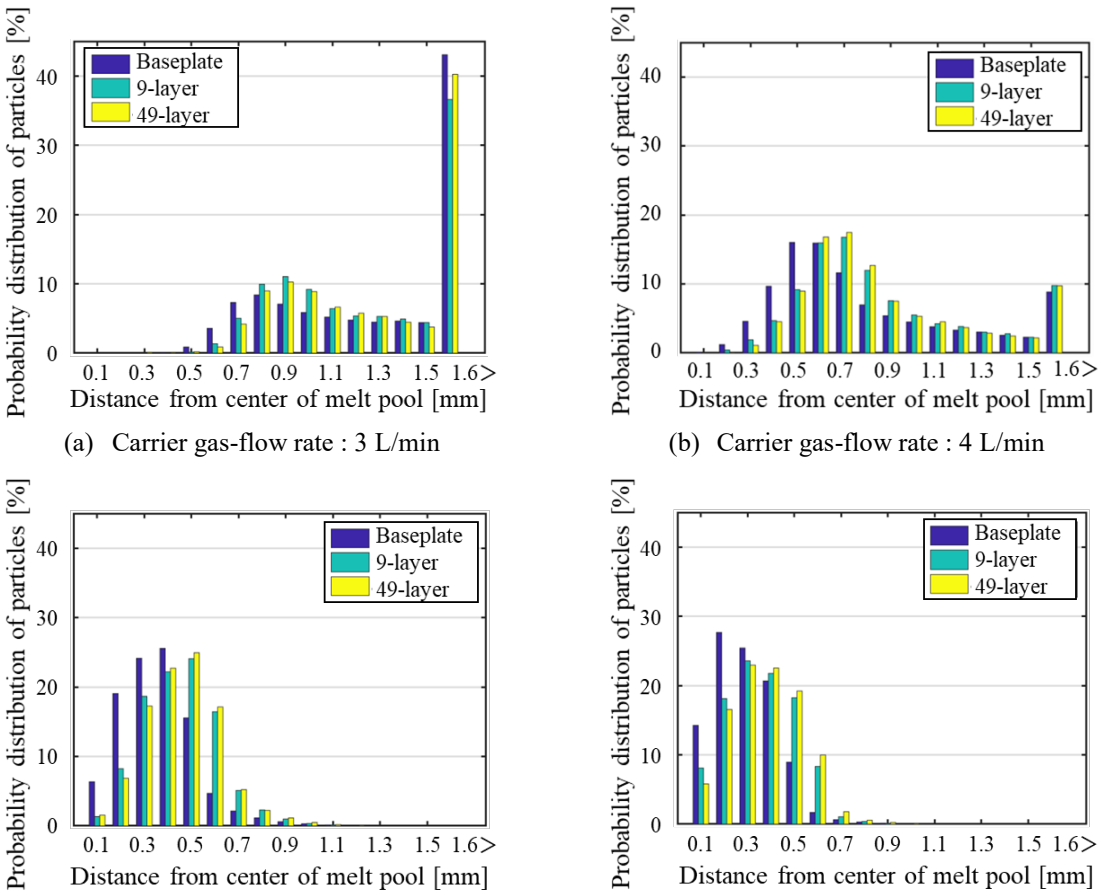

(a) Carrier gas-flow rate : 3 L/min (b) Carrier gas-flow rate : 4 L/min

(c) Carrier gas-flow rate : 6 L/min (d) Carrier gas-flow rate : 8 L/min

Figure 7: Probability distribution of particles

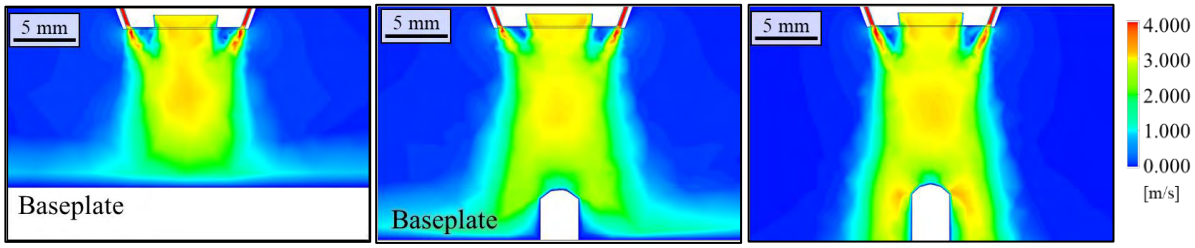

(a) Baseplate (b) 9-layer (c) 49-layer

Figure 8: Flow velocity distribution (Carrier gas-flow rate : 4 L/min)

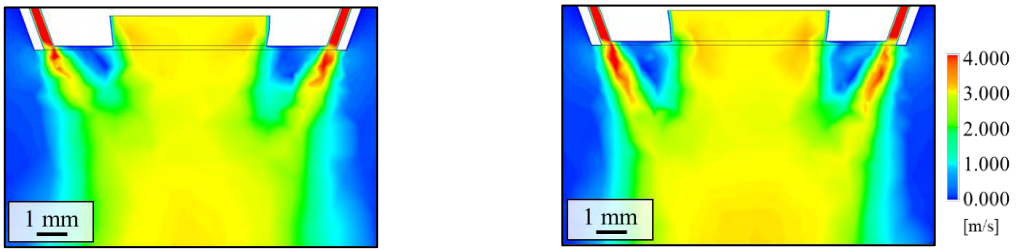

(a) 9-layer (b) 49-layer

Figure 9: Flow velocity distribution around nozzle exit

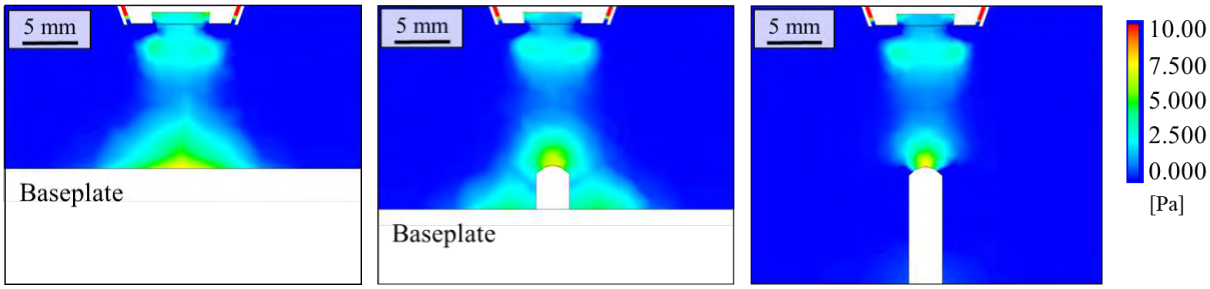

(a) No deposit (b) 9-layer (c) 49-layer

Figure 10: Pressure distribution (Carrier gas-flow rate : 4 L/min)

The velocity and pressure distributions represent that the distance from the top surface of deposit and the baseplate would affect the particle trajectory under the nozzle. Considering that the gas flow becomes downward in 49-layer deposition, some particles may reach at an off-center region. From these results, the gas-flow condition needs to be modified according to the deposition height for enhancing the stability of powder supply.

In addition, comparing the particle distribution shown in Fig. 7 regarding the carrier gas-flow rate, the particle convergence is more enhanced with larger carrier gas-flow rate regardless the deposition height. The average ratio of particles distributing within 1.5 mm from the center of melt pool in 3-type deposition heights ($= \bar{p}_{1.5}$) are 99.9% in the carrier gas-flow rate of 6 and 8 L/min, whereas the $\bar{p}_{1.5}$ are 60.0% and 90.5% in the carrier gas-flow rate of 3 and 4 L/min, respectively. As a result, the carrier gas-flow rate should be at least 6 L/min or more for high powder convergence with this powder nozzle when the deposition height changes.

5 MODIFICATION OF POWDER NOZZLE

The modification of the powder-nozzle shape is also considered. Although particles can be supplied to the melt pool when the carrier gas-flow rate is high as 6 L/min according to the simulation results, the higher carrier gas-flow rate drastically generates sputter. Moreover, in terms of cost and resource saving, a reduction of gas consumption is beneficial for DED. From the view point of the powder supply efficiency, which is a percentage of material actually used for the deposit, the powder convergence should be improved even with the low carrier gas-flow rate.

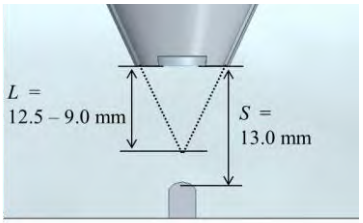

Figure 11: Cross-section of modified powder nozzle

The powder convergence distance L is changed in the coaxial powder nozzle in this simulation. Considering that the particles are hardly supplied into the center of melt pool in Fig. 6, the actual converged height would be below the designed height represented with the convergence distance L. From this reason, the convergence distance L is shorter than the standoff distance S in the new powder nozzle. Concretely, L is designed to be 9.0 – 12.5 mm at 0.5 mm intervals (Fig. 11), and the simulation conditions are same as Table 1, excepting the carrier gas-flow rate is set to be 4 L/min.

Figures 12 and 13 show the simulation results of the particle distribution on the XY coordinates when L = 10.5 and 11.0 mm, respectively. Comparing with Fig. 6, particles are supplied to the center of melt pool and the powder convergence would be improved with the new nozzles.

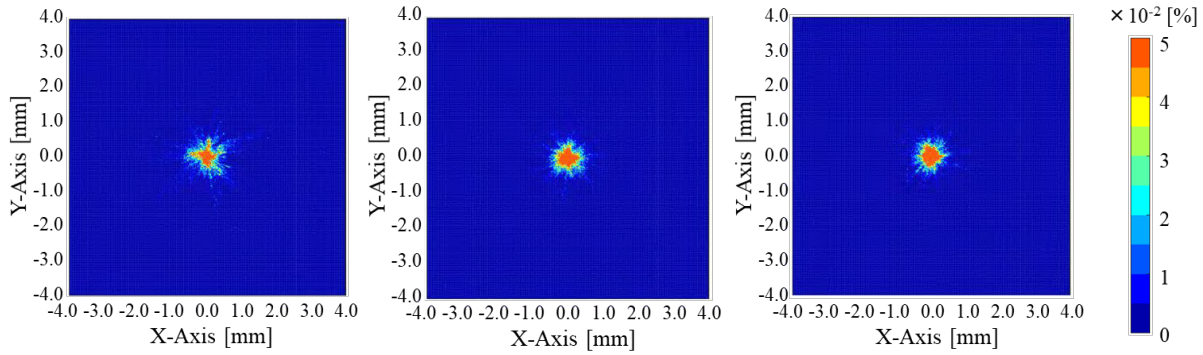

(a) Baseplate (b) 9-layer (c) 49-layer

Figure 12 Particle distribution on top surface of deposit and baseplate (Convergence distance : 10.5 mm)

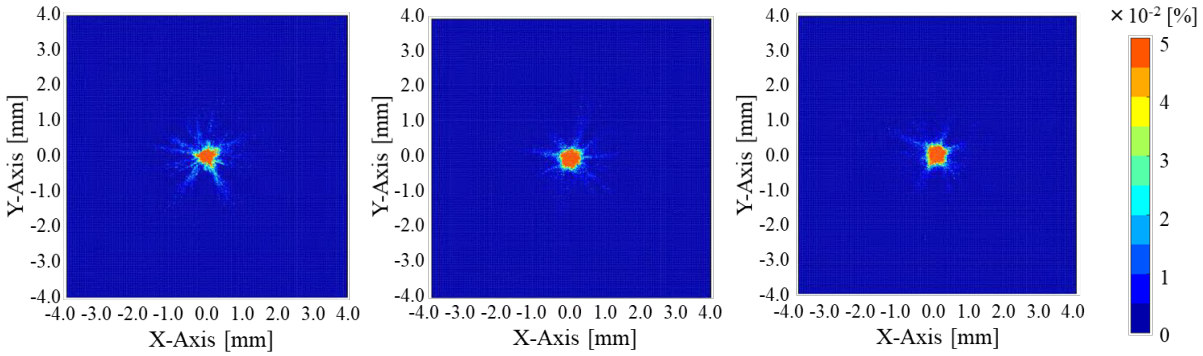

(a) Baseplate (b) 9-layer (c) 49-layer

Figure 13 Particle distribution on top surface of deposit and baseplate (Convergence distance : 11.0 mm)

Furthermore, Fig. 14 shows the probability distribution of particles when L = 10.5 and 11.0 mm. Comparing with Fig. 7(b), the powder distribution gets close to the center of melt pool, and $\bar{p}_{1.5}$ is improved to 94.8% and 93.3% respectively. Moreover, the expected distance between the center of melt pool and arrival point of particle (=E) is calculated. In the results of L = 10.5 mm, the expected distance E becomes 0.66, 0.46 and 0.43 mm on the baseplate, 9-

layer and 49-layer deposit respectively. In the results of L = 11.0 mm, the E becomes 0.70, 0.48 and 0.46 mm on the baseplate, 9-layer and 49-layer deposit respectively. The conventional nozzle with carrier gas-flow rate of 6 L/min (Fig. 7(c)) showed that the E was 0.36, 0.45 and 0.46 mm. From these results, the high particle convergence is achieved even with low carrier gas-flow rate in 9- and 49-layer deposit. On the other hand, the particle convergence on the baseplate is not improved enough when the carrier gas supply is small as 4 L/min.

In practical usage, an adjustment of the carrier gas-flow rate would be effective to achieve the stable powder convergence. The simulation is also conducted by using the new nozzle model (L = 10.5, 11.0 mm) with 6 L/min of carrier gas-flow rate, and the probability distribution of particle is obtain as shown in Fig. 15. In the both results with new nozzles, $p_{1.5}$ on the baseplate reaches 99.9 %. Therefore, the new nozzles can achieve the high particle convergence stably by supplying carrier gas of 6 L/min only for the deposition on a baseplate. Furthermore, the particle convergence is kept in high even with small carrier gas supply as 4 L/min during the deposition on higher layer. As a future work, experimental investigation needs to be conducted with the suggested nozzle design and carrier gas-flow rate corresponding to the vilification of simulation.

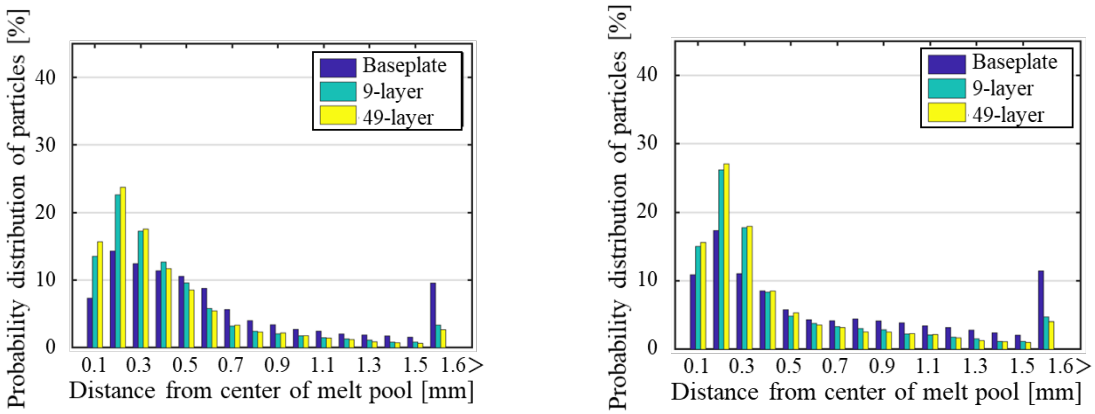

(a) Convergence distance L : 10.5 mm (b) Convergence distance L : 11.0 mm

Figure 14: Probability distribution of particles (Convergence distance : 10.5, 11.0 mm)

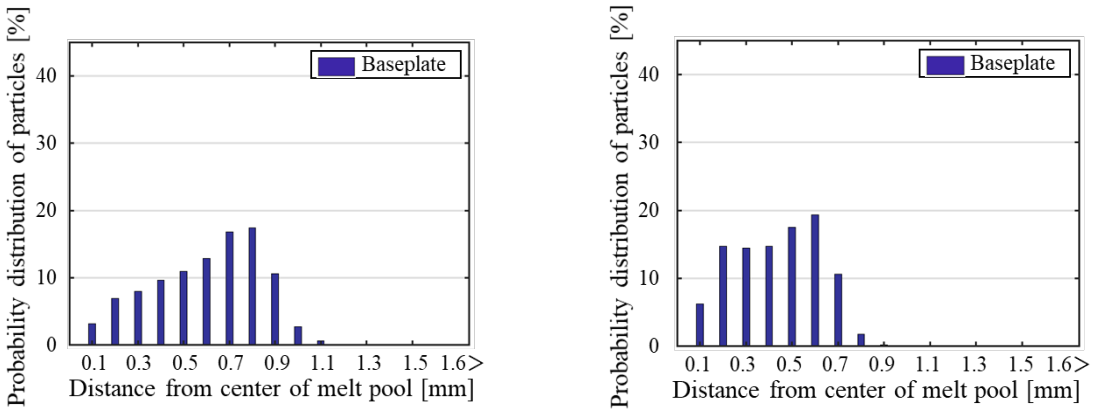

(a) Convergence distance L : 10.5 mm (b) Convergence distance L : 11.0 mm

Figure 15: Probability distribution of particles (Carrier gas-flow rate : 6 L/min)

6 CONCLUSIONS

An influence of carrier gas-flow rate and the deposition height on the particle distribution is investigated by conducting the computational fluid dynamics simulation. Furthermore, the design of powder-nozzle shape is discussed and evaluated numerically. The obtained results are summarized as follows:

- According to the simulation considering the deposit with various heights, the particle distribution slightly spreads when the deposit is higher. The analysis of the flow velocity and pressure distribution indicates that the distance from the top surface of deposit and baseplate affects the particle trajectory under the nozzle.
- In order to enhance the powder convergence even with low carrier gas supply, the powder-nozzle shape is changed by shortening the convergence distance L than the standoff distance S. In the results of L = 10.5 and 11.0 mm, $\bar{p}_{1.5}$ is improved to 94.8% and 93.3% respectively from the result in conventional nozzle of 90.5%.
- The powder convergence on the baseplate is still low. The simulation results indicate that the new nozzles can achieve the high convergence stably and reduce total amount of gas supply by increasing the carrier gas-flow rate only on the baseplate.

REFERENCES

[1] Michael, S. and Marion, M. et al. Laser based additive manufacturing in industry and academia, *CIRP Annals - Manufacturing Technology* (2017) **66**:561-583.
[2] James, C. H. and Baolong, Z. et al. Working distance passive stability in laser directed energy deposition, *Materials and Design* (2019) **161**:86-94.
[3] Heng, P. and Todd, S. et al. The Investigation of Gravity-Driven Metal Powder Flow in Coaxial Nozzle for Laser-Aided Direct Metal Deposition Process, *Journal of Manufacturing Science and Engineering* (2006) **128**:541–553.
[4] Gangxian, Z. and Dichen, L. et al. Numerical simulation of metallic powder flow in a coaxial nozzle in laser direct metal deposition, *Optics & Laser Technology* (2011) **43**:106–113.
[5] Arrizubieta, J. L. and Tabernero, I. et al. Continuous coaxial nozzle design for LMD based on numerical simulation, *Physics Procedia* (2014) **56**:429-438.
[6] Christopher, K. and Weixiao, S. st al. Modeling Particle Spray and Capture Efficiency for Direct Laser Deposition Using a Four Nozzle Powder Injection System, *Journal of Manufacturing Science and Engineering* (2018) **140**:041014.
[7] Zhang, B. and Coddet, C. Numerical study on the effect of pressure and nozzle dimension on particle distribution and velocity in laser cladding under vacuum base on CFD, *Journal of Manufacturing Processes* (2016) **23**:54-60.
[8] Uazir, D.O. and Vaclav, O. Analysis of coaxial laser cladding processing conditions, *Surface and Coatings Technology* (2005) **197**:127-136.
[9] B.E. Launder, Spalding DB. *Lectures in mathematical models of turbulence*. Academic Press, (1972).